Numerical Investigation of Supersonic Nozzle Flow Separation

Q. Xiao[*] and H.M. Tsai[†]
Temasek Laboratories, National University of Singapore, Singapore 119260, Singapore

and

D. Papamoschou [‡]
Department of Mechanical and Aerospace Engineering
University of California, Irvine CA 92697-3975, USA

.

The separated flow in a convergent-divergent (CD) nozzle is investigated by the solution of the Reynolds-Averaged Navier-Stokes equations with a two-equation k-ω turbulent model. For a fixed area ratio, defined as the exit area to the throat area, A_e/A_t of 1.5, computations are conducted over a range of nozzle pressure ratio (NPR). The case investigated experimentally by Papamoschou and Zill (2004) is used here to assess the computation. The computational results are used to further examine the effect of the separated flow. Unlike the experiment, no unsteady shock movements are simulated. However the computed wall pressure distribution is in good agreement with the experimental data. Also consistent with experimental observations, the flow separates asymmetrically for the range of 1.5<NPR<2.4 investigated. Further at higher NPR not covered by the experiment, the present computation shows the flow reverts to a symmetric form. The center-line pressure distribution shows a succession of expansion and compression waves after the main lambda shock confirming the conjectured model by Papamoschou and Zill (2004) based on Schlieren photography.

Nomenclature

A_e = nozzle exit area
A_t = nozzle throat area
A_s = nozzle area at shock location
M = Mach number
NPR = nozzle pressure ratio = P_{01}/ P_a
P_c = center-line pressure
P_{01} = total pressure at nozzle inlet
P_1 = static pressure before normal shock
P_2 = static pressure after normal shock
P_a = ambient pressure
x = stream-wise location
H_t = throat height

---

[*] Research Scientist, Temasek Laboratories, National University of Singapore, Singapore.
[†] Principal Research Scientist, Temasek Laboratories, National University of Singapore, Singapore, Member AIAA.
[‡] Professor, Department of Mechanical and Aerospace Engineering, University of California, Irvine, California, USA, Associate Fellow AIAA.

I. Introduction

Flow separation may occur in an over-expanded convergent-divergent (CD) nozzle due to the nozzle expansion ratio being too large for a given nozzle pressure ratio (NPR). In that case, supersonic nozzle flow expands to a pressure level that is far lower than the ambient pressure, causing the formation of a normal shock and detachment of the ensuing flow from the nozzle walls. For some nozzle shapes, the flow separation can generate large unpredictable side-loads. The earlier studies considered the separation as an undesirable occurrence, and showed that off-design nozzle thrust efficiency could be greatly improved by controlling the location and extent of the separation. Recent investigations by Papamoschou[1], Murakami and Papamoschou[2] and Papamoschou et al.[3] show that separated nozzle flows can be explored for their potential application in the fluid mixing. The understanding and prediction of the physical mechanisms behind the supersonic nozzle separation flow is important for designing efficient nozzle configuration that avoids asymmetric side forces and enhances flow mixing.

Although there is a large amount of literature published for separated nozzle as Ref 4-6, the detailed investigation on separation flow mechanism is less matured. Most of available publications are concentrated on prediction of separation location. A review paper by Morrisette and Goldberg[4] based on a variety of experimental results concludes that zero-pressure gradient separation prediction method, like that proposed by Reshotoko and Tucker[5], give reasonable predictions for nozzles with turbulent separation and large divergence angle. In the paper of Romine[6], the mechanism for causing the flow separation from the nozzle wall is demonstrated, and the theory for a new solution of the separation location is presented. It is noted that a complicated shock structure in the separated jet is observed during the pressure adjustment process. Near the center-line of the nozzle, Romine[6] postulates that the pressure adjusts to the ambient pressure via a gradual underexpansion. On the wall, the flow adjusts to the ambient pressure almost immediately past the shock.

Some previous studies have conducted numerical prediction of separated nozzle flows and the internal performance, such as Hunter[7], Carlson[8], Xiao et al.[9-10]. In general, their computation is in excellent agreement with experimental data. In the paper of Hunter[7], two distinct separation regimes are shown from their experimental results on a two-dimensional planar nozzle with A_e/A_t =1.8. For NPR<1.8, the flow shows three-dimensional separation with partial reattachment. Fully-detached two-dimensional separation is found for NPR>2.0. The underexpansion of flow after the main shock is evident from the computed Mach number contours, although this was not explicitly expressed.

Recently, Papamoschou and Zill[11] investigated experimentally the supersonic separated flow inside a symmetric convergent-divergent nozzle. The study is motivated by the occurrence of mixing enhancement outside CD nozzle operated at low pressure ratio. Their preliminary study found that for large area ratio $A_e/A_t \geq 1.4$ and nozzle pressure ratio NPR>1.4, the flow pattern could be asymmetric, that is: a well-defined lambda shock with one foot is always larger than the other. The asymmetry does not flip during a given test run, but can change side from run to run. The flow downstream of the Mach stem expands to near-sonic speed and exhibits an alternation of subsonic and supersonic regions. The experimental measurements of centerline pressure distribution are qualitatively consistent with their flow mechanism conjecture. It is also found that for large A_e/A_t and NPR, the shock is unsteady without resonant tones.

The asymmetric lambda shock occurring in geometrically symmetric nozzle has not been computed. Deck et al.[12] conducted the computation for a supersonic asymmetric planar nozzle investigated in ONERA S8Ch wind tunnel. The nozzle has two throats, the second throat, of adjustable cross section, locates downstream of the test section, can induce the partial starting of the nozzle and generate separation shock structure. Unsteady Reynolds-averaged Navier-Stokes equations with Spalart-Allmaras turbulent model was used for the computation. Depending on the throat contraction ratios, defined as the ratio of two throat height, stable symmetric and asymmetric lambda shock patterns are obtained.

The detailed investigation of fundamental flow separation mechanism for over-expanded convergent-divergent nozzle is less mature. The aim of the present paper is to examine the supersonic nozzle flow separation. The experiment by Papamoschou and Zill[11] of a two-dimensional symmetric convergent-divergent nozzle forms the basis for comparison. The results are used for better understanding the physics of flow structure inside the supersonic separated nozzle and detect the cause of the asymmetry of this phenomenon.

In the following sections, the governing equations and the numerical methods are outlined briefly. This is followed by the discussion of the numerical results. The conclusions will be made in the final section.

II. Numerical Method

The governing equations for the unsteady compressible turbulent flow are expressed as follows:

Mass conservation:
$$\frac{\partial \rho}{\partial t}+\frac{\partial}{\partial x_j}(\rho u_j)=0 \tag{1}$$

Momentum conservation:
$$\frac{\partial}{\partial t}(\rho u_i)+\frac{\partial}{\partial x_j}(\rho u_j u_i)=-\frac{\partial p}{\partial x_i}+\frac{\partial \hat{\tau}_{ji}}{\partial x_j} \tag{2}$$

Mean energy conservation:
$$\frac{\partial}{\partial t}(\rho E)+\frac{\partial}{\partial x_j}(\rho u_j H)=\frac{\partial}{\partial x_j}\left[u_i\hat{\tau}_{ij}+(\mu+\sigma^*\mu_T)\frac{\partial k}{\partial x_j}-q_j\right] \tag{3}$$

Turbulent mixing energy:
$$\frac{\partial}{\partial t}(\rho k)+\frac{\partial}{\partial x_j}(\rho u_j k)=\tau_{ij}\frac{\partial u_i}{\partial x_j}-\beta^*\rho\omega k+\frac{\partial}{\partial x_j}\left[(\mu+\sigma^*\mu_T)\frac{\partial k}{\partial x_j}\right] \tag{4}$$

Specific dissipation rate:
$$\frac{\partial}{\partial t}(\rho\omega)+\frac{\partial}{\partial x_j}(\rho u_j\omega)=(\varepsilon\omega/k)\tau_{ij}\frac{\partial u_i}{\partial x_j}-\beta\rho\omega^2+\frac{\partial}{\partial x_j}\left[(\mu+\sigma\mu_T)\frac{\partial \omega}{\partial x_j}\right] \tag{5}$$

where t is time, x_i position vector, ρ is the density, u_i velocity vector, p pressure, μ dynamic molecular viscosity, ν_{tE} kinematic equilibrium turbulent eddy viscosity, k turbulent mixing energy, and ω the specific dissipation rate. The total energy and enthalpy are $E=e+k+u_iu_i/2$ and $H=h+k+u_iu_i/2$, respectively, with $h=e+p/\rho$ and $e=p/[(\gamma-1)\rho]$. The term γ is the ratio of specific heats. Other quantities are defined in the following equations:

$$\mu_T=\rho\nu_t \tag{6}$$

$$\nu_{tE}=\varepsilon^* k/\omega \tag{7}$$

$$S_{ij}=\frac{1}{2}\left(\frac{\partial u_i}{\partial x_j}+\frac{\partial u_j}{\partial x_i}\right) \tag{8}$$

$$\tau_{ij}=2\mu_T\left(S_{ij}-\frac{1}{3}\frac{\partial u_k}{\partial x_k}\delta_{ij}\right)-\frac{2}{3}\rho k\delta_{ij} \tag{9}$$

$$\hat{\tau}_{ij}=2\mu\left(S_{ij}-\frac{1}{3}\frac{\partial u_k}{\partial x_k}\delta_{ij}\right)+\tau_{ij} \tag{10}$$

$$q_j=-\left(\frac{\mu}{\mathrm{Pr}_L}+\frac{\mu_T}{\mathrm{Pr}_T}\right)\frac{\partial h}{\partial x_j} \tag{11}$$

Where Pr_L and Pr_T are the laminar and turbulent Prandtl numbers, respectively. The other coefficients are: $a_0=0.35$, $\varepsilon=5/9$, $\varepsilon^*=1$, $\beta=0.075$, $\beta^*=0.09$, $\sigma=0.5$, $\sigma^*=0.5$.

The basic numerical method used to solve the above system of equations in this paper follows that described in detail by Sadeghi et al.[13] A cell-centered finite volume scheme is used to discretize the governing equations. The k and ω variables are defined at cell centers in a similar fashion to the main flow quantities. A central difference scheme is used to discretize the diffusive terms. A scalar dissipation scheme (JST) scheme is used for convective terms in the Navier-Stokes equation. A second-order MUSCL-type up-winding scheme is applied for the k-ω equations. A multiblock grid topology is used to discretize the flow field and parallel computing is implemented with MPI to exchange the information within different blocks.

After being discretized in space, the governing equations are reduced to a set of ordinary differential equations with only derivatives in time, which can be solved using a multi-stage Runge-Kutta type scheme. Here, a 5-stage scheme is used. The artificial dissipation is updated at stages 1, 3 and 5. Local pseudo-time stepping is used in order to advance the flow solution at the local maximum speed. Residual smoothing is applied at stages 1, 3 and 5 in order to increase the stability limit. A multigrid method is adopted to accelerate the convergence of the solution. Dual-time stepping method is used for the unsteady time-marching.

III. Results and Discussions

The same planar 2D convergent-divergent supersonic nozzle tested by Papamoschou and Zill[11] is studied here. Computations are conducted and compared with the experimental data from Ref. 7 for NPR between 1.269 and 2.4. The computed area ratio A_e/A_t is fixed at 1.5.

The computational domain includes the domain inside the nozzle and an ambient region around the outer surface and downstream of the nozzle with 10 throat-heights downstream, upstream and normal to the jet axis. Fig. 1 shows the geometry and grid distribution. The grid density is higher in the divergent part of the nozzle to improve the resolution for capturing the shocks. The grid is clustering to the top and bottom walls. The number of the grid points inside the nozzle is 236 x 85. Grid dependence testing (not shown here) verifies this grid is sufficient fine for capturing the main flow characteristics inside the nozzle. For a Reynolds number based on the throat height of 5.5 million, the minimum first grid point from the wall gives a $y^+<1$. The boundary conditions are imposed as follows: the total pressure and total temperature at the nozzle inlet are set to be $p_t = NPR \times p_a$, $T_t = T_a$, respectively, where p_a is the ambient pressure equal to 14.85 psi and T_a is the ambient temperature set at 290K. The no-slip boundary conditions are specified for the nozzle top and bottom walls. The ambient pressure and free-stream Mach number (Ma=0.1) are set along the outer surface of the computational domain.

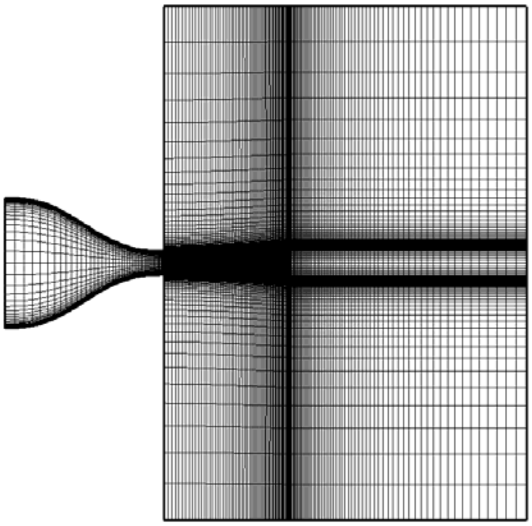

Figure 1. Computational domain and mesh.

The simulation is initially conducted with unsteady computation with dual-time stepping method. However, the convergence history and computed shock location shows the flow to assume a steady state. The cause of this is not entirely clear. Generally in the computation with time-stepping method, if the solution converges without any periodic oscillation in the residual, it is a good indication that the phenomenon is steady. This is particular so if one uses RANS time-averaged computation which does not handle any random unsteadiness. The computation is then carried out with steady method. The typical convergent history of maximum residual of momentum equation at NPR=1.612 is presented in Fig. 2. At least 2 to 3 orders of residual reduction are obtained. A good convergence of a steady computation indicates that no unsteady phenomenon could be calculated with unsteady methods. Therefore, the results presented below are obtained by the steady computation with varied CFL numbers from 2.0 to 4.0.

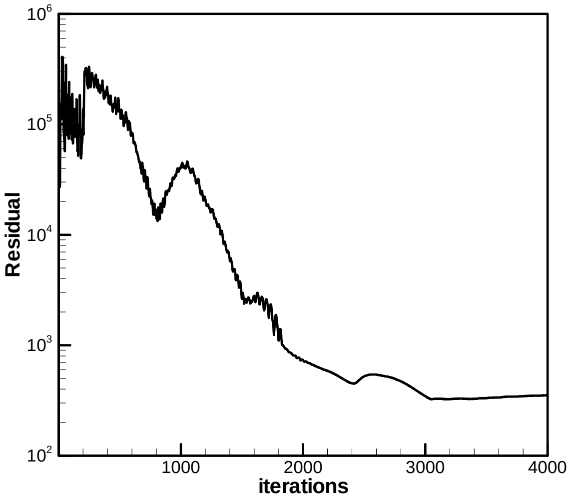

Figure 2. Convergent history of maximum residual.

Flow Pattern

The computed Mach contours for NPR values from 1.269 to 2.4 are shown in Figs. 3(a)-(g). Note that the nozzle exist is located at $x/H_t \approx 5.0$. It is seen that a well-defined lambda shock appears inside the nozzle for all NPR values. Each lambda foot is characterized by the incident shock, reflected shock, and the triple point where the incident and reflected shocks merge into the Mach stem. For NPR>1.30, nozzles are operated in an over-expanded condition, as indicated by the earlier separation of the flow. The point of separation moves away from the nozzle throat as the nozzle pressure ratio increases. One important feature is that, for 2.4 > NPR > 1.5, the lambda shock is asymmetric with a large foot occurrence at one side wall. Beyond this range, the shock is symmetry. This is consistence with the experimental work of Papamoschou and Zill[11] typically shown in Fig.4(a) and Fig.5(a).

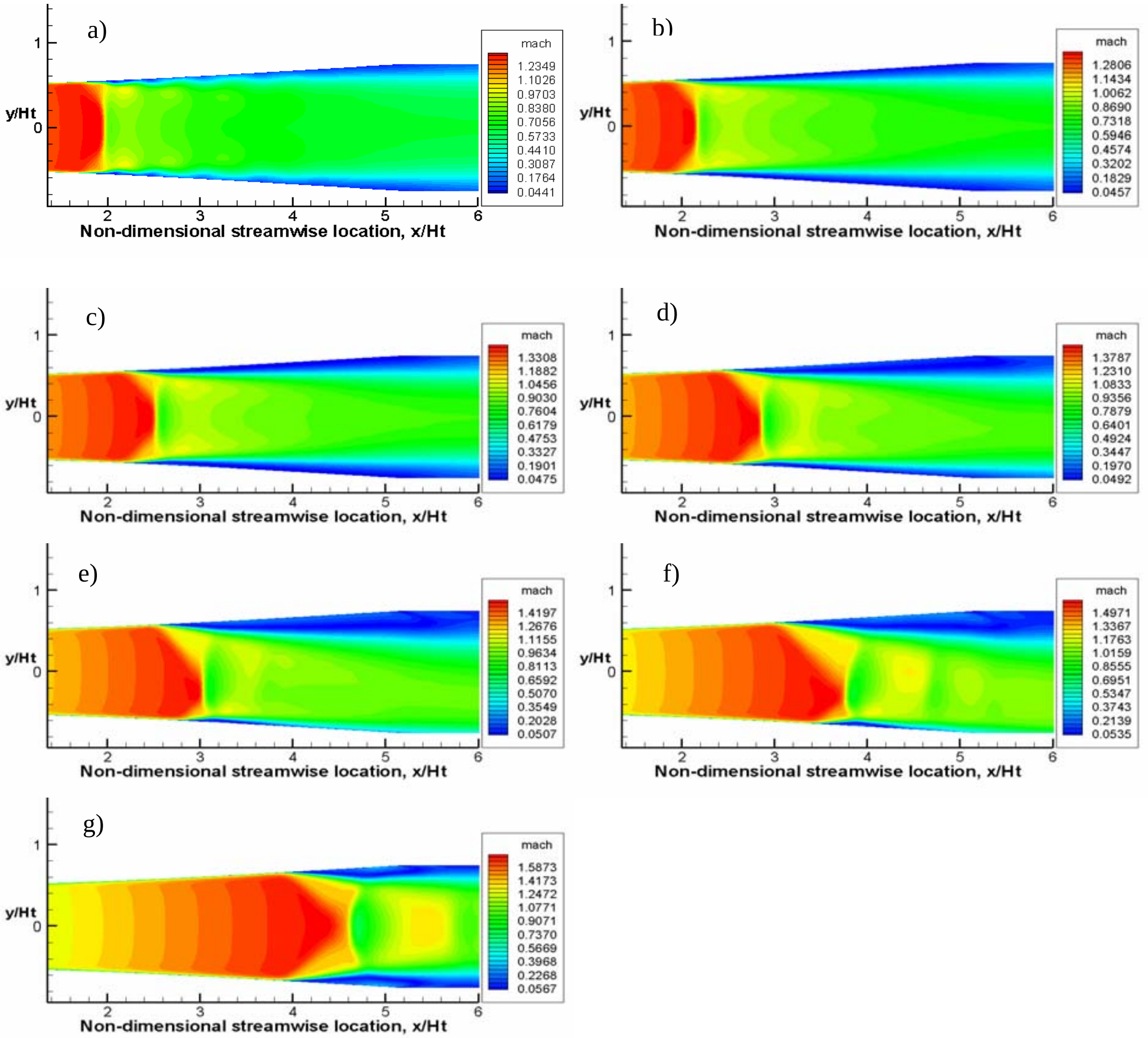

Figure 3. Mach number contours at different NPR values for A_e/A_t =1.5. (a) NPR=1.269 (b) NPR=1.30 (c) NPR=1.50 (d) NPR=1.612 (e) NPR=1.70 (f) NPR=2.0 (g) NPR=2.4.

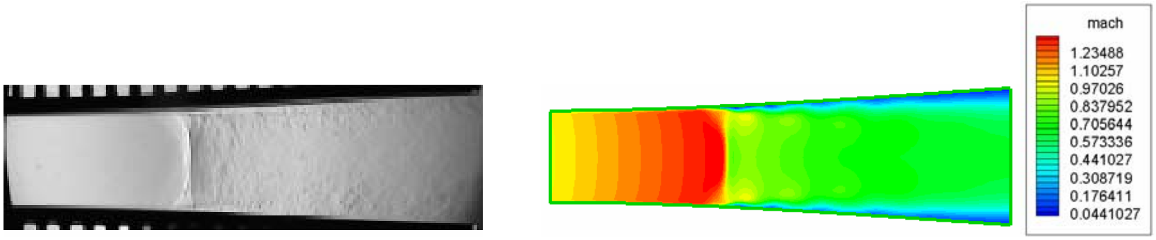

a) b)

Figure 4. Comparison of flow pattern for NPR=1.269. (Symmetric lambda shock) (a) Experimental Schlieren flow visualization picture; (b) Computational Mach number contour.

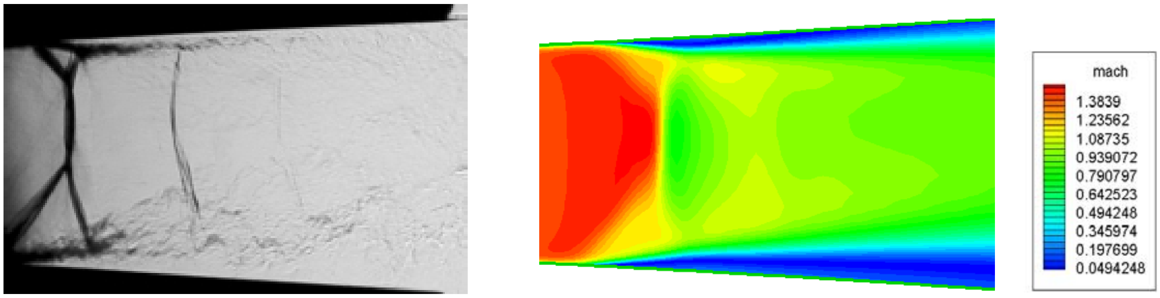

a) b)

Figure 5. Comparison of flow pattern for NPR=1.612. (Asymmetric lambda shock) (a) Experimental Schlieren flow visualization picture; (b) Computational Mach number contour.

Further investigation for the flow asymmetry is conducted. It is found that larger lambda shock of the asymmetrical pattern could be forced either on the top or on the bottom wall by means of perturbation placed near one wall. The perturbation is imposed by setting a normal velocity near one side of the wall on the initial flow field. The magnitude of the velocity is about 5% of the mean flow velocity. The existence of three shock patterns at same area ratio for A_e/A_t=1.5 and NPR=1.612 are shown in Fig. 6. Three shock patterns are all stable and the shock locations are the same. The perturbation method is applied over a range of NPRs investigated. It is found that for the same amount of perturbation, the asymmetry becomes more obvious with increasing of NPR as shown in Fig.3. However, when NPR reaches 2.4, the asymmetry disappears. It is clear that this bifurcation phenomenon only exists in a particular range of NPR.

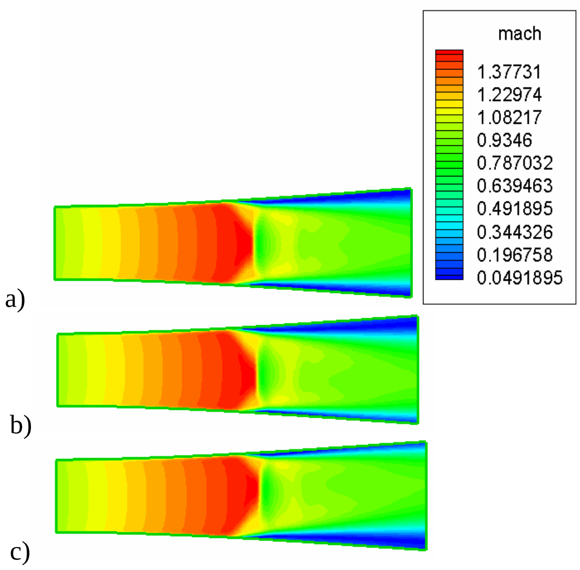

Figure 6. Mach number contour for three different shock wave at A_e/A_t=1.5 and NPR=1.612. (a) Symmetry shock (b) Asymmetric lambda shock with large foot at top wall (c) Asymmetric lambda shock with large foot at bottom wall.

The contours of statistical turbulent kinetic energy: $k = \frac{1}{2}(\overline{u'^2} + \overline{v'^2} + \overline{w'^2})$, normalized by reference velocity defined as $u_{ref} = \sqrt{\gamma R T_0}$ where T_0 is the total pressure at the nozzle inlet plane, are presented in Fig. 7 for different NPR. The two separated areas after the lambda shock are the seat of a high level of k/u_{ref}^2 due to the presence of fully turbulent mixing layers. In the central region of the nozzle, the flow is rather invisid. Refer to Fig. 3, the maximum intensity is obtained in the region with detached mixing layer close to the interaction with the reflection of large foot of lambda shock. Downstream of the reattachment points, these levels decrease. With the increasing of NPR from 1.269 to 2.4, the maximum turbulent intensity level increases about 3.2 times, and the location of the maximum turbulent intensity also moves downstream towards the nozzle exit plane.

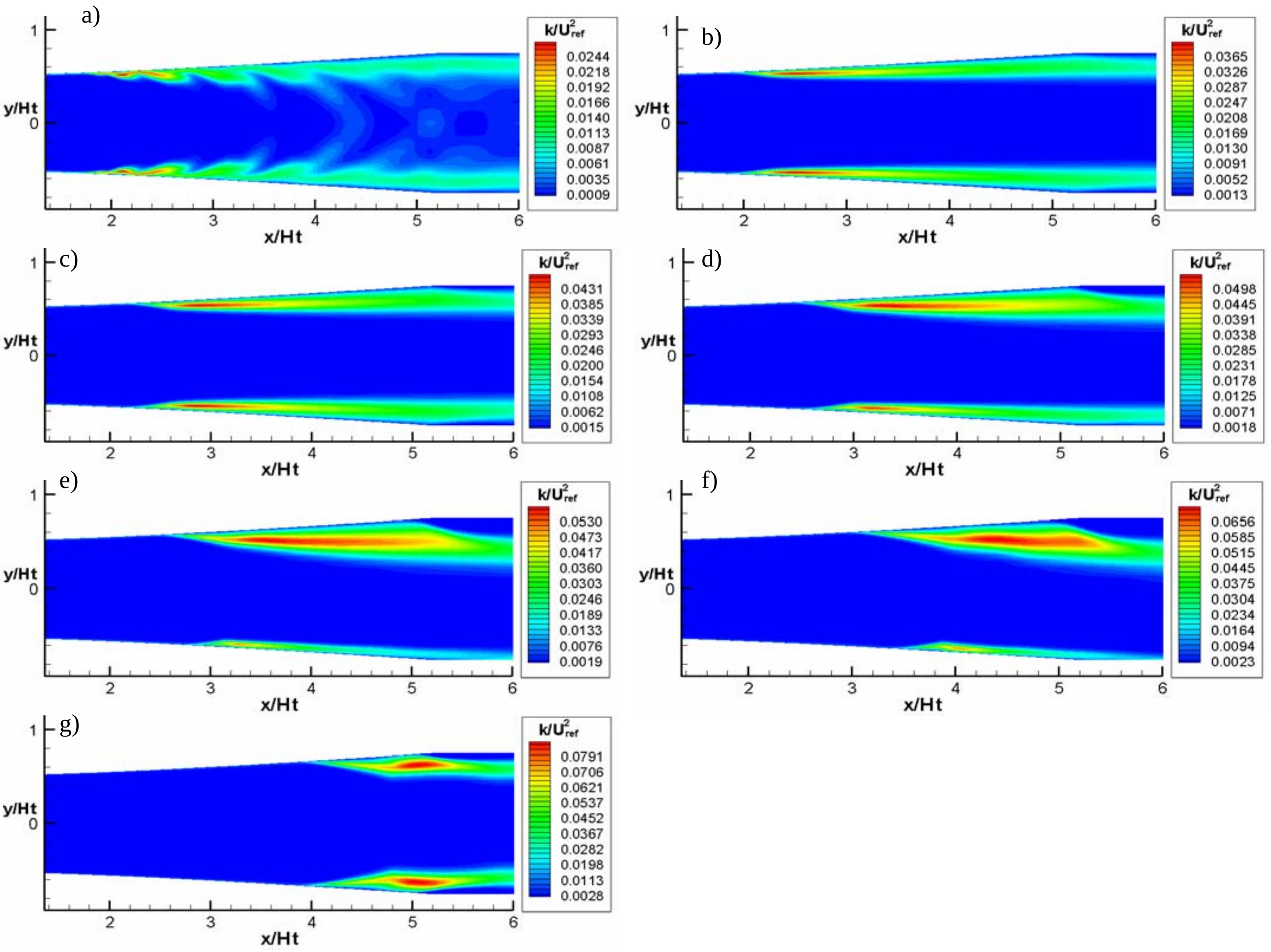

Figure 7. Turbulent kinetic energy contour at different NPR. (a) NPR=1.269 (b) NPR=1.30 (c) NPR=1.50 (d) NPR=1.612 (e) NPR=1.70 (f) NPR=2.0 (g) NPR=2.4

As Figures 3 and 7 indicate that, for large NPR, separation is asymmetric, with the large separation region occurring on the side with large lambda shock foot. Flow separates at the origin of the incident oblique shock and forms a wavy shear layer that bounds the recirculation region. The reflected branch of the lambda shock further reflects from the shear layer and forms an expansion wave. The typical streamline after the lambda shock and separation region for NPR=1.70 is shown in Fig.8.

The evolution of the shock position A_S/A_t is presented in Fig. 9 for computational and experimental data. A_S/A_t is defined as the area ratio corresponding to the axial position of the Mach stem (normal shock) of the main shock divided by the throat area. As seen from the figure, the computations are in good agreement with the experimental data for available experimental data. The scatter of the experimental data around NPR=1.6 is caused by the unsteadiness of the shock motion. The computations here do not predict any such shock oscillations.

Wall Pressure Distribution

The computed top wall pressure distribution along with the experimental data is shown in Fig.10. The pressures are normalized by the nozzle inlet total pressure. As shown from the figure, the computed pressure distributions are in good agreement with experiments. The pressure distributions have the "classic" shape of expansion, shock jump, and recovery. For lower NPRs, the pressure downstream of the shock recovers to the ambient pressure in a smooth gradual way. For NPR = 2.0, and 2.4, the recovery of pressure is more immediately compared to the lower NPRs.

In the theoretical work of Romine[6], the flow near the wall is assumed to adjust to the ambient pressure almost immediately past the shock. This is only partially valid here for large NPRs like 2.0 and 2.4. As seen from the Mach number contours in Fig. 3, for NPR = 2.0 and 2.4, the shock locates near the nozzle exit. For lower NPR, the underexpansion is evident in the Mach number contour, therefore the pressure recovers to the ambient pressure in a gradual way.

The comparison of top and bottom wall pressure distributions for NPR = 1.269 and NPR = 1.612 are shown in Fig. 11 along with the experimental data. For lower NPR values like 1.269, since the lambda shock is symmetric, there are no noticeable differences between top and bottom wall. However, for large NPR like 1.612, significant differences exist between the top and bottom walls as a result of the asymmetric

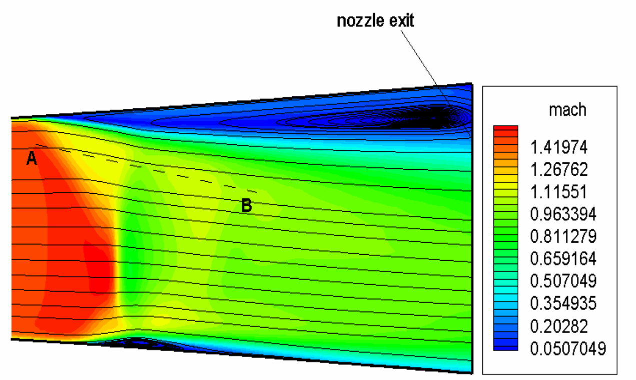

Figure 8. Streamline and separation region for NPR=1.70.

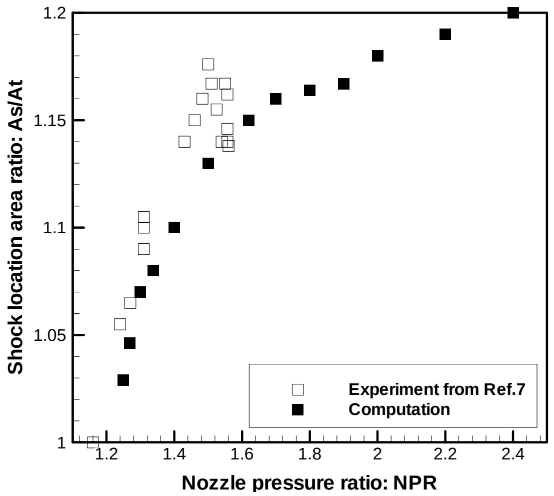

Figure 9. Shock location variation with nozzle pressure ratio.

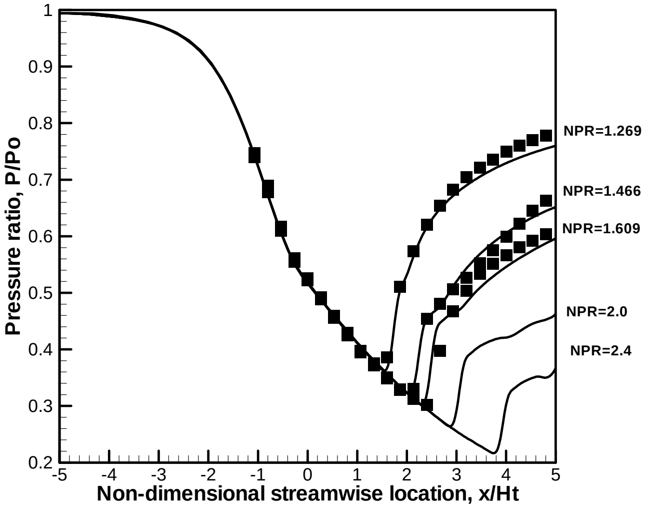

Figure 10. Comparison of top wall pressure distribution. Symbols: experiment (Ref.7); lines: computation.

shock pattern occurrence. As seen from the figure, after the shock, the pressure recovers linearly with axial distance for the top wall where the large lambda shock foot exists. The pressure shows a faster initial rise followed by a gradual recovery to ambient value on the bottom wall where the small foot occurs. Papamoschou and Zill[11] found the same behavior in their experiments.

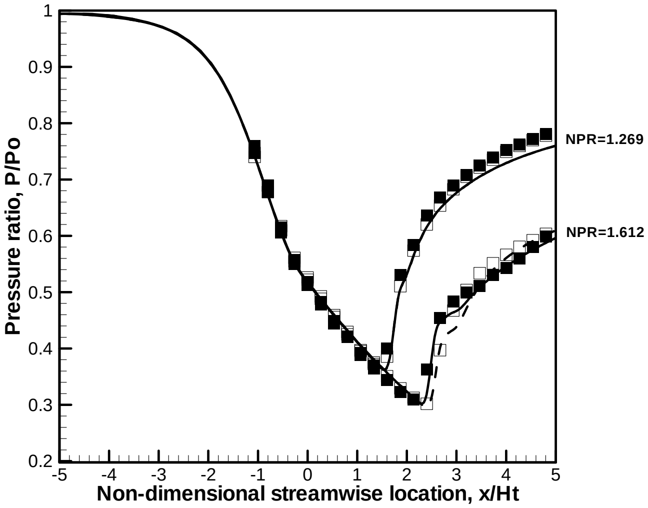

Figure 11. Top and bottom wall pressure distribution. Lines: computation; (Dash: bottom wall; Solid: top wall) Symbols: Experiments. (Ref.7) (Open: top wall; Close: bottom wall)

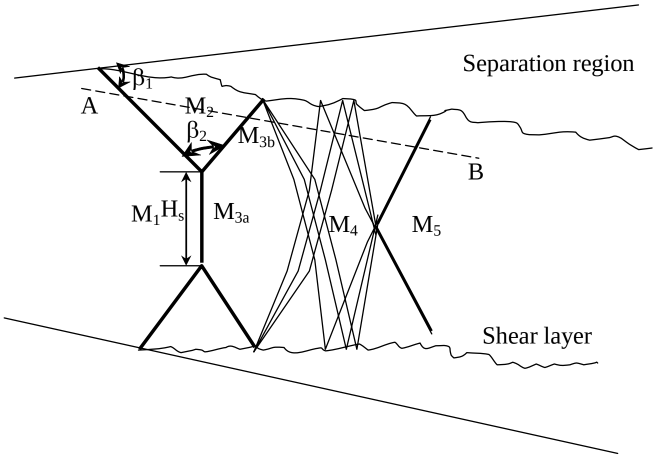

Figure 12. Schematic of shock and flow structure.

Shock Structure

Apart from the above observation, a succession of weak waves past the main shock is presented in Fig.3 for large NPRs. The flow immediately downstream of the main shock accelerates to supersonic speed, recompresses, and then reaccelerates. The sketch of the successive shock pattern and flow structure as proposed by Papamoschou and Zill[11] is examined here in Fig. 12 where M and β are the Mach number and shock angle, respectively. Subscripts 1 and 2 denote the conditions immediately before the Mach sterm and after the incident oblique shock, respectively. Subscripts 3a and 3b represent the conditions after the Mach stem and reflected oblique shock, respectively. Subscripts 4 and 5 represent the condition after the expansion and compression, respectively, following the main shock. To illustrate the interaction between the shock and boundary layer, the shock measurements are made from the computed results, and summarized in Table 1 where H_s is the height of the normal shock and H_t is the height of the throat.

Table 1 Effect of NPR on the shock structure.

NPR	β_1	β_2	M_1	M_2	M_{3a}	M_{3b}	M_4	M_5	H_s/H_t	Lambda shock pattern
1.269	40°	82°	1.23	1.08	0.70	0.94	/	/	0.637	symmetry
1.338	48°	64°	1.41	1.09	0.78	0.98	0.921	0.736	0.545	symmetry
1.50	48°	65°	1.46	1.15	0.774	1.01	0.982	0.813	0.509	symmetry
1.609	48°	70°	1.53	1.15	0.778	1.02	1.086	0.887	0.454	asymmetry
1.7	50°	70°	1.61	1.15	0.77	1.02	1.07	0.942	0.424	asymmetry
2.0	45°	70°	1.65	1.25	0.816	1.03	1.21	0.976	0.409	asymmetry
2.3	43°	75°	1.67	1.31	0.82	1.04	/	/	0.31	asymmetry
2.4	42°	80°	1.69	1.34	0.84	1.05	/	/	0.1	symmetry

As seen from Table 1 and Fig. 3, the turning angle of the incident oblique shock β_1 increases with NPR and then decreases. No systematic change of reflection oblique shock β_2 by NPR is obtained. The height of the normal shock decreases monotonically with increasing of NPR. This trend is similar to the experimental observation.

The nozzle center-line Mach number distribution for different NPRs is shown in Fig. 13. The expansion immediately after the Mach stem is clearly seen for all NPRs. A successive recompression and expansion waves are obtained for large NPR like 1.609 and 1.7.

For a better understanding of the flow structure, the Mach number distribution along the nozzle center-line and along line AB (shown in Figs.8 and 12) are presented in Fig.14 for NPR=1.70. As seen from Table 1 and Fig.14, the flow after the incident oblique shock is supersonic, as M_2 indicates. For NPR≥1.50, there is a significant difference between the flow just after reflected shock and after the Mach stem. The flow downstream of the reflected shock is supersonic, as indicated by M_{3b}, while the flow past the Mach stem is subsonic (M_{3a}). The two regions are separated by a wavy slipstream. This phenomenon is not as pronounced at low NPR values. The flow after the main shock accelerates further by action of an expansion wave (M_4) and compresses by means of a weak shock (M_5). Generally, two to three successive expansion/shock systems past the main shock are observed in the computational results.

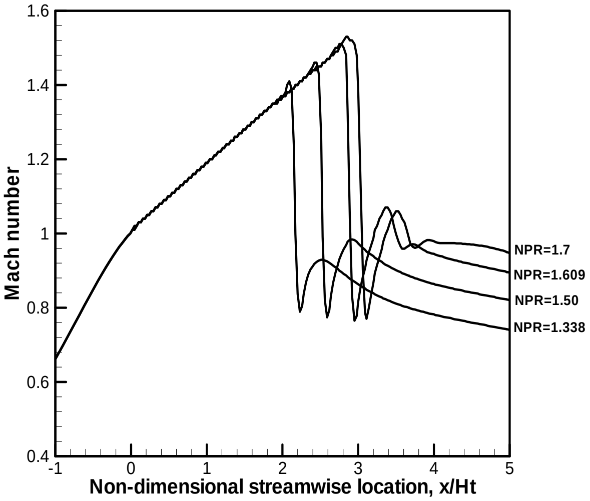

Figure 13. Center-line Mach number distribution.

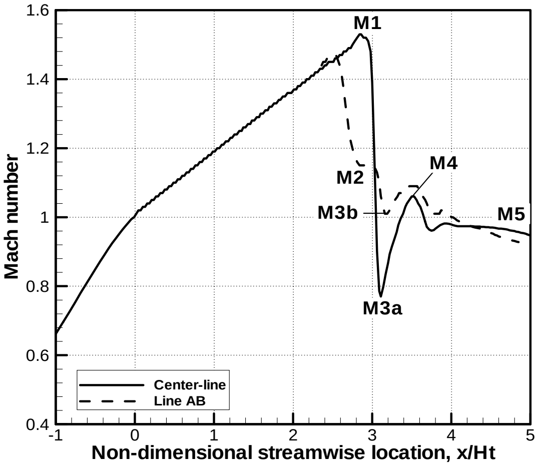

Figure 14. Mach number distribution along center-line and line AB (shown in Fig. 8 & 12) for NPR=1.70.

More evidence for supporting the flow structure displayed in Fig.12 can be obtained from the nozzle center-line pressure distribution shown in Fig. 15. Compared to the wall pressure distribution shown in Fig.10, the trend of center-line pressure distribution is similar to the wall pressure except that the pressure after the shock displays a dip, followed by a gradual rise to the ambient pressure. This indicates an under expansion immediately after the shock stem and before the compression. This is more pronounced for larger NPR values. In the experimental work of Papamoschou and Zill[11], they also found similar phenomenon for $A_e/A_t = 1.5$ and NPR = 1.51 as shown in Fig.16. However, the pressure dip after the shock is less significant than the computed pressure distribution. They postulated that this was due to the motion of the unsteady shock which smoothed the measured pressure distribution. The occurrence of pressure dip from computation is consistent with the flow sketch plotted in Fig. 12. The presence of shocks past the main shock indicates that the flow downstream of main shock accelerates to locally supersonic values. This is accomplished by the slipstream forming a sonic throat and then diverging. Further downstream, the slipstream creates additional sonic throat until it decelerates to subsonic Mach numbers. Romine's theory (Ref. 6) assumes that jet flow emerging from the shock is above ambient pressure and adjusts to the ambient pressure via a gradual underexpansion. Our results here confirm this argument and denote that this is applicable in the vicinity of the nozzle center-line where the shock is normal.

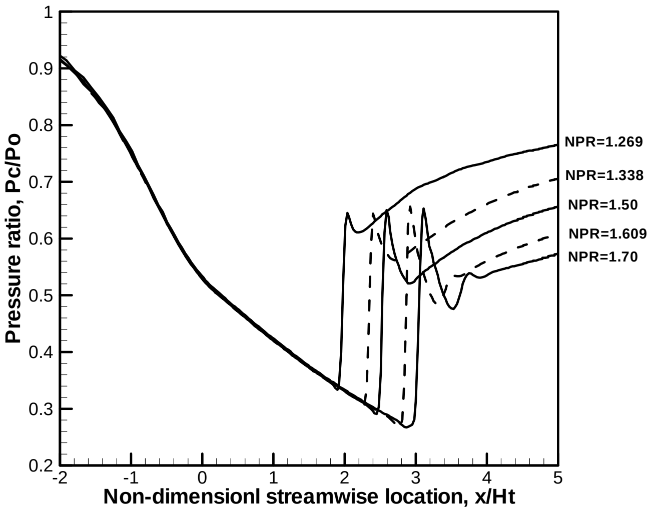

Figure 15. Computed center-line pressure distribution.

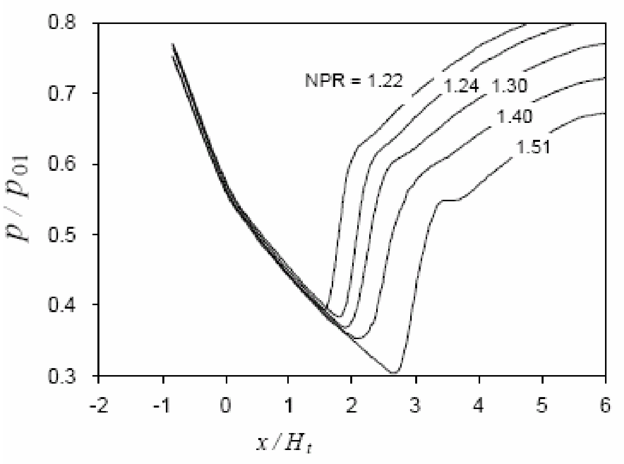

Figure 16. Measured center-line pressure distribution. (From Ref.7)

The center-line pressure distribution merits further discussion. Unlike the complex shock near the wall, the shock near center-line is a normal shock for NPR<2.4. The pressure rise across the shock follows the normal shock relation:

$$\frac{p_2}{p_1} = 1 + \frac{2\gamma}{\gamma + 1}\left(M_1^2 - 1\right) \tag{12}$$

where M_1 is the flow Mach number immediately upstream of the shock and p_1 and p_2 are the static pressure before and after the normal shock, respectively. The relation of static pressure p_1 and total pressure p_{01} follows:

$$\frac{p_1}{p_{01}} = (1 + \frac{\gamma - 1}{2} M_1^2)^{\frac{-\gamma}{\gamma - 1}} \tag{13}$$

Combining Eq.(12) and Eq.(13), we obtain the following relation for p_2:

$$\frac{p_2}{p_{01}} = \frac{4\gamma}{\gamma^2 - 1}\left(\frac{p_1}{p_{01}}\right)^{\frac{1}{\gamma}} - \frac{(\gamma + 1)^2}{\gamma^2 - 1}(\frac{p_1}{p_{01}}) \tag{14}$$

The Eq. (14) is plotted in Fig. 17 along with the experimental data and computational results. As seen from the figure, the computed pressure is much closer to the theory compared to the experiments. In fact, as shown in Fig.16, the experimentally measured pressure rise across the shock is much lower than the normal-shock relation as represented by Eq. (12). As pointed out by Papamoschou and Zill[11], this is due to the fact that center-line pressure probe does not measure the true pressure distribution but a filtered distribution due to the oscillation which reduces the pressure rise. The hypothetical pressure distribution discussed in Ref. 7 which does not include Gaussian smoothing is consistent with the computational results and normal shock relationship.

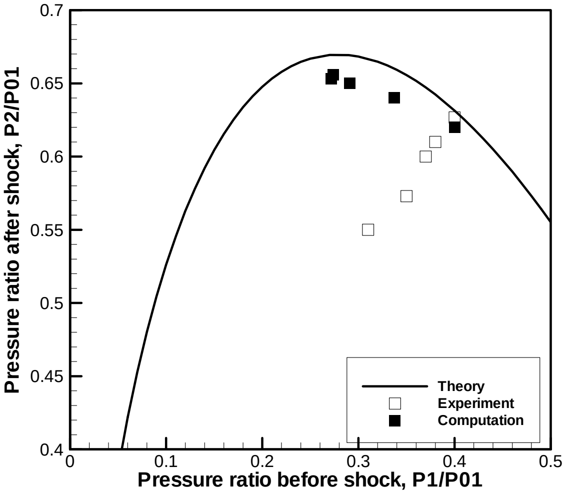

Figure 17. Comparison of normal shock relation for the center-line pressure before and after the shock.

IV. Conclusion

The separated flow in a convergent-divergent (CD) nozzle is computationally studied here for the case of $A_e/A_t = 1.5$, over a range of NPR. The simulation is conducted using the Reynolds-averaged Navier-Stokes equation with two-equation k-ω turbulence model. The experimental data by Papamoschou and Zill[11] is used here to assess the computational results and further examine the flow physics of asymmetric separated flow in symmetric nozzle. The following conclusions can be drawn:

1. Unlike the experiment, no unsteady shock movements are captured despite attempts to time resolve any unsteady motion in the flow. In all computations made here, the flow converges to a steady state. This may be in line with the experimental observation that there is no distinct resonant tone indicating a possible lack of acoustic feedback mechanism. The possible difference of the computation to capture the unsteady motion of the shock may indicate that the motion is random.

2. Consistent with experimental observations, the flow separates asymmetrically for the range $1.5<NPR<2.4$ investigated. Two lambda shocks are observed as in the experiment with one being larger than the other. The present results show that, the asymmetry of the shock disappears for larger NPR. With increasing NPR the shock moves downstream and towards the nozzle exit plane.

3. The measured mean center-line pressure is smeared out by the shock motion and thus do not reflect the actual pressure level in the flow structure. However the computed center-line pressure distribution provides strong evidence of a succession of expansion and compression waves after the main lambda shock. This basic flow structure of shock and boundary layer interaction, conjectured by Papamoschou and Zill[11], based on the qualitative observations from Schlieren photography is confirmed by the present computation.

4. For $NPR<1.609$, the computed wall pressure distribution is in good agreement with the experiment, which shows a gradual pressure recovery to the ambient pressure after the oblique shock. For NPR = 2.0 and 2.4, which are beyond the experimental range, the computational wall pressure distribution shows an almost immediately recovery of the wall pressure as the shock occur further down-stream near the nozzle exit. This is consistent with Romine's theory which states that the wall pressure adjusts to the ambient pressure immediately after the shock on the wall. For the NPR values which is less than 1.609, this generalization by Ronnie is not applicable.

5. The size of the separated flow region is clearly evident from the computation. For the asymmetric flow the separated flow region is a dominant part of the flow inside the nozzle exhibiting higher turbulence level. The scale of the separated flow region extends towards the nozzle exit plane. The turbulent intensity also increases with NPR. Such asymmetric flow field feature can be readily captured by the RANS computation.

References

[1] Papamoschou, D., "Mixing Enhancement Using Axial Flow," AIAA-2000-0093, 1993.
[2] Murakami, E. and Papamoschou, D., "Experiments on Mixing Enhancement in Dual-Stream Jets," AIAA-2001-0668, 2001.
[3] Papamoschou, D., Dixon, T. D., and Nishi, K., "Mean Flow of Multi-Stream Rectangular Jets under Normal and Mixing-Enhancement Conditions." AIAA-2004-0919, 2004.
[4] Morrisette, E. L., and Goldberg, T. J., "Turbulent Flow Separation Criteria for Over-Expanded Supersonic Nozzles," NASA TP 1207, Aug. 1978.
[5] Reshotko,E., and Tucker, M., "Effect of a Discontinuity on Turbulent Boundary Layer Thickness Parameters with Application to Shock-Induced Separation," NACA TN-3454, 1955.
[6] Romine, G. L., "Nozzle Flow Separation," *AIAA Journal*, Vol. 36, No.9, pp.1618-1625, 1998.
[7] Hunter, C.A., "Experimental, Theoretical, and Computational Investigation of Separated Nozzle Flows" AIAA-98-3107 1998.

[8] Carlson, J.R., “A Nozzle Internal Performance Prediction Method,” NASA Technical Paper 3221, 1992.

[9] Xiao,Q, Tsai, H. M., and Liu, F. “Computation of Transonic Diffuser Flows by a Lagged k-ω Turbulence Model”, *Journal of Propulsion and Power*, Vol. 19, No.3, pp.473-483, 2003.

[10] Xiao,Q, Tsai, H. M., and Liu, F. “Computation of Turbulent Separated Nozzle Flow by a Lag Model”, *Journal of Propulsion and Power*, Vol.21, No.2, pp.368-371, 2005.

[11] Papamoschou, D. and Zill A., “Fundamental Investigation of Supersonic Nozzle Flow Separation”, AIAA-2004-1111, 2004.

[12] Deck, S., Hollard, R. and Guillen, Ph. “Numerical Simulation of Steady and Unsteady Separated Nozzle Flows”, AIAA-2002-0406, 2002.

[13] Sadeghi, M., Yang, S., Liu, F., and Tsai, H. M., “Parallel Computation of Wing Flutter with a Coupled Navier-Stokes and CSD Method” AIAA-2003-1347, 2003.